







Sediment supply controls on Early Eocene delta sequences (South Pyrenean Foreland Basin; Spain)

Romain Vaucher^{1,2*} , Claire Musajo², Jorge E. Spangenberg³ , Miquel Poyatos-Moré⁴ , Christian Zeeden⁵ ,
Cai Puigdefàbregas⁶, Sébastien Castelltort¹ , Thierry Adatte² 

¹ Department of Earth Sciences, University of Geneva, Rue des Maraîchers 13, 1205 Geneva, Switzerland

² Institute of Earth Sciences (ISTE), University of Lausanne, Geopolis, 1015 Lausanne, Switzerland

³ Institute of Earth Surface Dynamics (IDYST), Géopolis, University of Lausanne, 1015 Lausanne, Switzerland

⁴ Departament de Geologia, Universitat Autònoma de Barcelona, 08193 Cerdanyola del Vallés, Spain

⁵ Leibniz Institute for Applied Geophysics (LIAG), Geozentrum Hannover, Hannover, Germany

⁶ Department of Earth and Ocean Dynamics, University of Barcelona, C/ Martí i Franquès, s/n, 08028 Barcelona, Spain

*Corresponding author: romain.vaucher88@gmail.com
[@RomainVaucher](https://twitter.com/RomainVaucher)

ABSTRACT

Sediment supply variations are often overlooked when interpreting depositional sequences, which tend to emphasize changes in accommodation. Here, we focus on a temporally well-constrained shallow-marine succession in the South Pyrenean Foreland Basin to test the control of sediment supply on the development of deltaic sequences during the Early Eocene. We analyzed the paleoenvironmental record (sedimentary facies and $\delta^{13}\text{C}_{\text{org}}$ values) of the Morillo Limestone and the Castigaleu Formation (52.2 to 50.3 Ma). During this period, a series of hyperthermal events occurred, globally recorded as negative carbon isotopic excursions (CIEs). The major progradation of the deltaic system is marked by the abrupt appearance of thick delta-front sandstones and coincides with the first recorded negative CIE. Subsequent phases of progradation/aggradation align with subsequent negative CIEs. Conversely, positive CIEs correspond to finer-grained, more distal prodelta and offshore deposits. We therefore suggest that during deposition of this Early Eocene shallow-marine succession, the primary trigger behind sequence generation was the high-frequency climate-induced variation in sediment supply, specifically the hyperthermal events, rather than changes in accommodation. This linkage underscores the complex interactions between climate dynamics and sedimentary responses, shaping the stratigraphic architecture of shallow-marine settings.

INTRODUCTION

Accommodation changes (δA) are often emphasized as the dominant control of depositional sequences (Burgess, 2016). However, according to sequence stratigraphic principles, sediment supply variations (δS) can also generate sequences (Jervey, 1988; Schlager, 1993; Muto and Steel, 1997; Burgess and Prince, 2015; Zhang et al., 2019). Accommodation is influenced by factors such as subsidence, tectonic activity, sea-level fluctuations, and sediment compaction (Jervey, 1988), which are more easily measured and analyzed than sediment supply budgets and variations (Allen et al., 2013). In addition, δS integrates a wide range of complex factors, including sediment fluxes from rivers, sediment transport processes, and local sediment sources, all exhibiting considerable temporal and spatial variability linked to climate conditions and fluctuations (Catuneanu

et al., 2009). Disentangling the influence of δA and δS on the origin of stratigraphic sequences, therefore poses significant challenges in interpretation, mainly due to the non-unique control of the resulting stratigraphic pattern (Burgess and Prince, 2015).

Here, we analyzed paleoenvironmental variations recorded in an Early Eocene shallow-marine succession of the South Pyrenean Foreland Basin (SPFB) (Fig. 1) to investigate whether sediment supply can be a dominant factor generating deltaic sequences. The Early Eocene Climate Optimum (EECO; 53.26 to 49.14 Ma) was characterized by a hothouse climate with high atmospheric CO_2 concentrations, elevated temperatures, and ice-free poles (e.g., Westerhold et al., 2020). Additionally, the EECO was marked by several hyperthermal events involving abrupt and substantial releases of isotopically depleted carbon

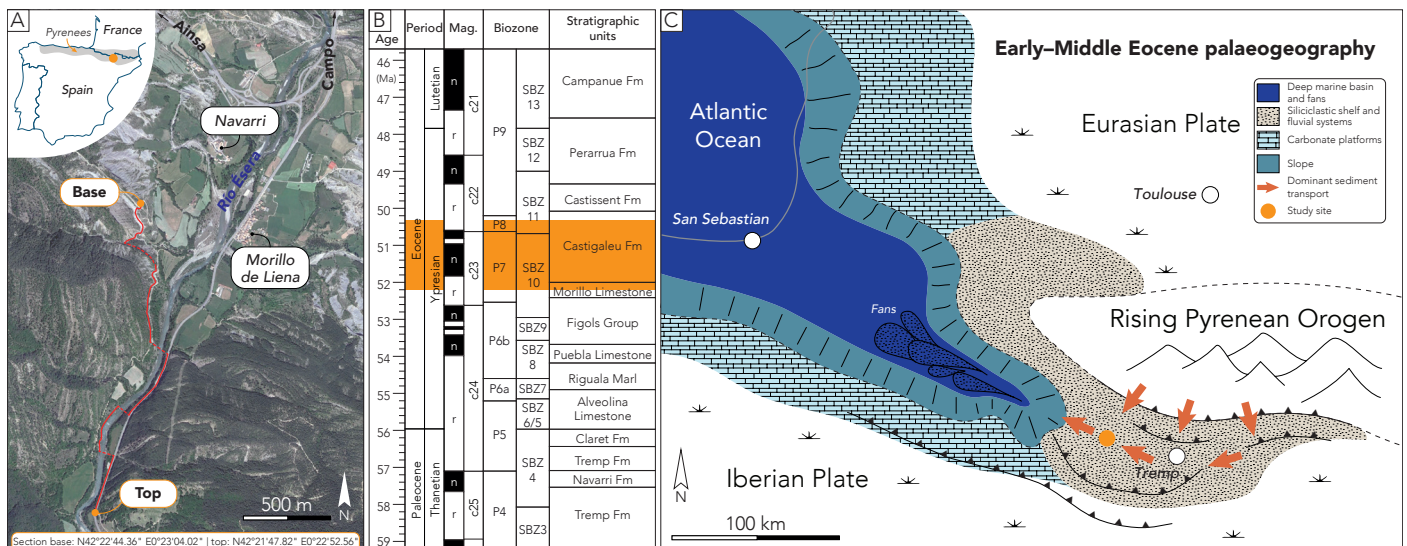


Figure 1. A) Map of the study area near Navarri, Spain. The red line indicates the section logged along the Río Ésera. B) Chronostratigraphic diagram of the Tresp-Graus Basin during the Paleocene-Eocene epochs (after Chanvry et al., 2018 and references therein). The studied interval is shown in orange. n: normal. r: reversed. C) Simplified reconstruction of the Pyrenean area during the Early-Middle Eocene (after Payros et al., 2009; Castellort et al., 2017).

into the ocean-atmosphere system. Hyperthermal events are evidenced by distinctive negative carbon isotope excursions (CIEs) observed globally in sedimentary records (Westerhold et al., 2020). By analogy with the Paleocene-Eocene Thermal Maximum (PETM) (Foreman et al., 2012; Chen et al., 2018; Vimperc et al., 2023) and the Middle Eocene Climate Optimum (MECO) (Peris Cabré et al., 2023), which are warming events showing increasing clastic sediment delivery to the ocean, therefore we anticipate similar sedimentary responses during the EECO. The combination of limited eustatic variability and possible high sediment supply variability creates favorable conditions to assess the role of sediment supply as a driver for stratigraphic sequences.

GEOLOGICAL SETTING

The Pyrenees (Fig. 1) formed as a result of the collision and subsequent subduction of the Iberian plate under the Eurasian plate (Ford et al., 2022). This orogeny took place from the late Cretaceous to the early Miocene, leading to the development of south-directed thrust sheets and duplex structures, including the Axial Zone and the South Pyrenean Central Unit (SPCU) (Muñoz, 1992). The major thrusts constituting the SPCU are the Bóixols, Montsec, and Serres Marginals, which detached in Triassic evaporite-rich levels (Puigdefàbregas and Souquet, 1986). From north to south, the Bóixols, Montsec, and Serres Marginals thrusts have led to the development of piggyback depocenters consisting of Mesozoic and Cenozoic deposits, namely, the Organyà, Tresp-Graus, and Àger basins (Muñoz et al., 2013), which collectively form the SPFB. The Early Eocene Morillo Limestone and the Castigaleu Formation (Fig. 1A, B) deposited within the Tresp-Graus Basin (Fig. 1C) and were the focus of this study. The chronostratigraphic framework for these stratigraphic units along the study area was previously established via magneto- and biostratigraphy (Bentham and Burbank, 1996).

METHODS

A 643.5 m thick stratigraphic section along the Río Ésera near Navarri (Spain) was logged and sampled ($n=293$) (Figs. 1–3). Stratal thicknesses were measured and a description was made of bed geometries, bounding contacts, grain size, sedimentary structures, ichnology and fossils (Figs. 2 and 3). Samples were collected in sandstone and mudstone 50 cm below the surface, cleaned, dried, and crushed. The organic carbon isotopic ratio ($\delta^{13}\text{C}_{\text{org}}$, ‰ VPDB) was measured on decarbonated samples using an elemental analyzer (Carlo Erba 1108 EA) coupled with an isotope ratio mass spectrometer (Thermo Fisher Scientific Delta V Plus) at the Institute of Earth Surface Dynamics of the University of Lausanne (UNIL), following the protocol described in Spangenberg (2016). $\delta^{13}\text{C}_{\text{org}}$ values were used to generate a local climate record comparable to global reference curves rather than $\delta^{13}\text{C}_{\text{carb}}$ values, which may have been affected by diagenetic and lithological effects, and because global trends in $\delta^{13}\text{C}_{\text{org}}$ mimic those of $\delta^{13}\text{C}_{\text{carb}}$, as previously demonstrated (McCarren et al., 2008; Khozyem et al., 2013). Whole-rock organic matter was analyzed using a Rock-Eval 6 (calibrated with IFP 160000 standard) at the Institute of Earth Sciences (UNIL) (Espitalie et al., 1985). The Rock-Eval pyrolysis allows determining the hydrogen and oxygen indices (HI, OI), T_{max} and the total organic carbon (TOC) content. $\delta^{13}\text{C}_{\text{org}}$ and Rock-Eval results are provided as Supplemental Material¹.

DEPOSITIONAL SETTINGS AND GEOCHEMISTRY

In the lower part of the studied section, bioclast-rich limestone beds (containing benthic foraminifera, oysters, and echinoderms) with a packstone to wackestone texture constitute the Morillo Limestone and also occur sporadically up section within the Castigaleu Formation (Figs. 2A and 3). These limestone beds record deposition in mid-ramp platform environments (Chanvry et al., 2018). On top of these, a large-scale coarsening-upward trend is observed, marking the transition to the Castigaleu Formation (Figs.

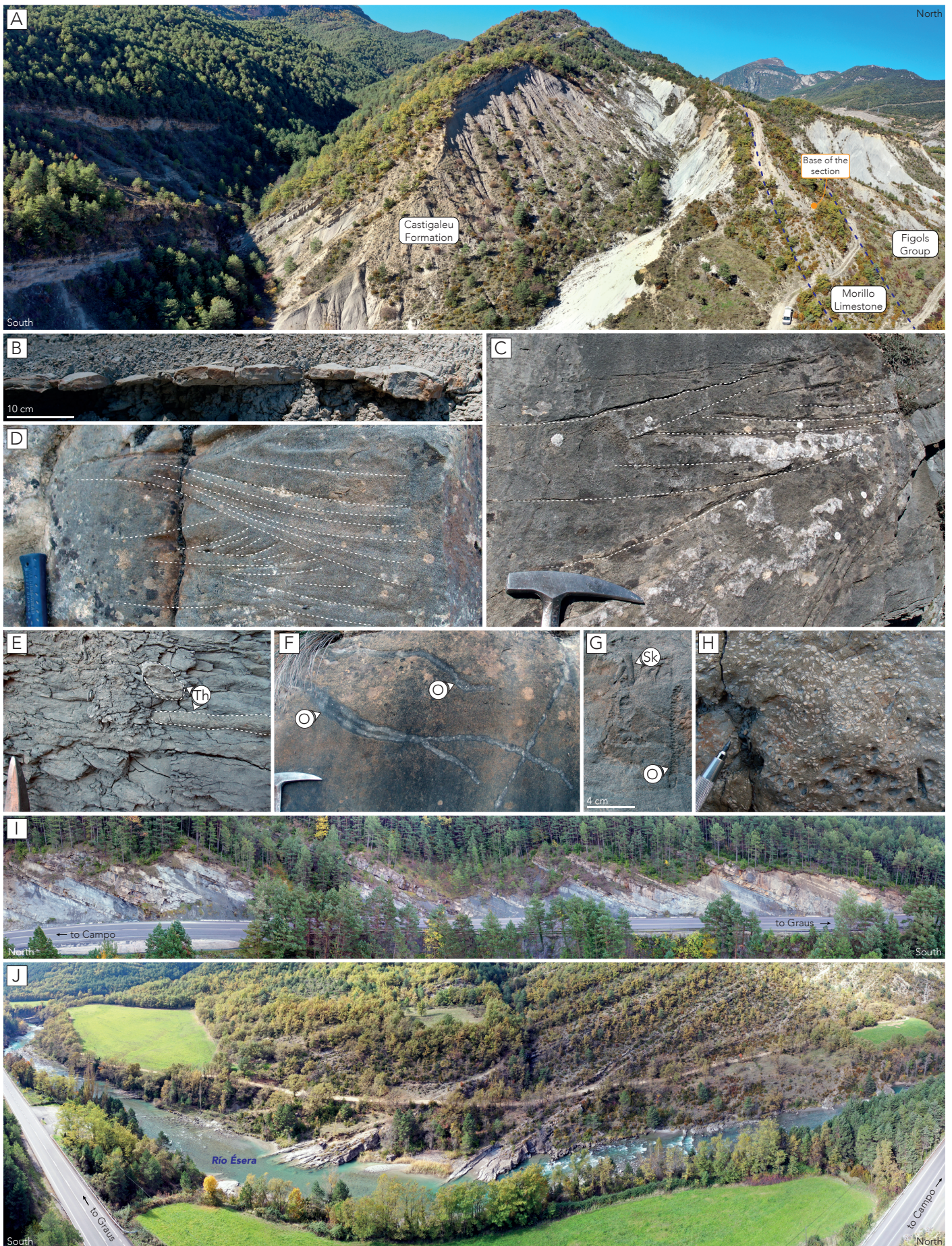


Figure 2. A) The transition from the Morillo Limestone to the Castigaleu Formation. B) Fine-grained, hummocky cross-stratified sandstone interbedded within a massive to laminated mudstone interval. C) Fine-grained, cross-bedded sandstone exhibiting single and double mud drapes on foresets and symmetrical cross-lamination are also present. D) Fine-grained, low-angle trough cross-bedded sandstone, with mud drapes on foresets. E) *Thalassinoides* (Th) traces within a massive silty mudstone. F) Large oblique *Ophiomorpha* (O) traces within fine-grained cross-bedded sandstones. G) *Skolithos* (Sk) and *Ophiomorpha* (O) traces within a massive to laminated medium-grained sandstone. H) Accumulation of benthic foraminifera, predominantly comprising *Nummulites* and *Alveolina*. I) The middle part of the section illustrates the recurrent alternation between cross-stratified sandstones and massive to laminated mudstones. J) Overview of the upper part of the studied section.

2A and 3). A progressive increase in cross-bedded sandstones interbedded with laminated to massive mudstones characterizes this transition (Figs. 2A-E and 3). Sandstone beds have sharp bases and occasionally show hummocky cross-stratification (Fig. 2D) but are predominantly massive or trough cross-stratified with single or double mud drapes on the foresets (Fig. 2D, C). Wood debris was also found. Bioturbation in sandstones and mudstones is sparse (Figs. 2F-H). Meter-thick massive to laminated mudstones frequently occurred and occasionally recorded accumulations

of large benthic foraminifera (Fig. 2H). The middle part of the Castigaleu Formation shows repeated alternations of cross-bedded sandstones and mudstones (Figs. 2I and 3) and a large-scale fining-upward trend (Figs. 2J and 3). These observations suggest that deposition occurred in a deltaic to shallow-marine environment, where massive to laminated mudstones with interbedded sandstone layers point to deeper-water prodelta and offshore settings. In contrast, cross-stratified sandstone beds reflect shallower subtidal bar and tide-influenced delta front deposits

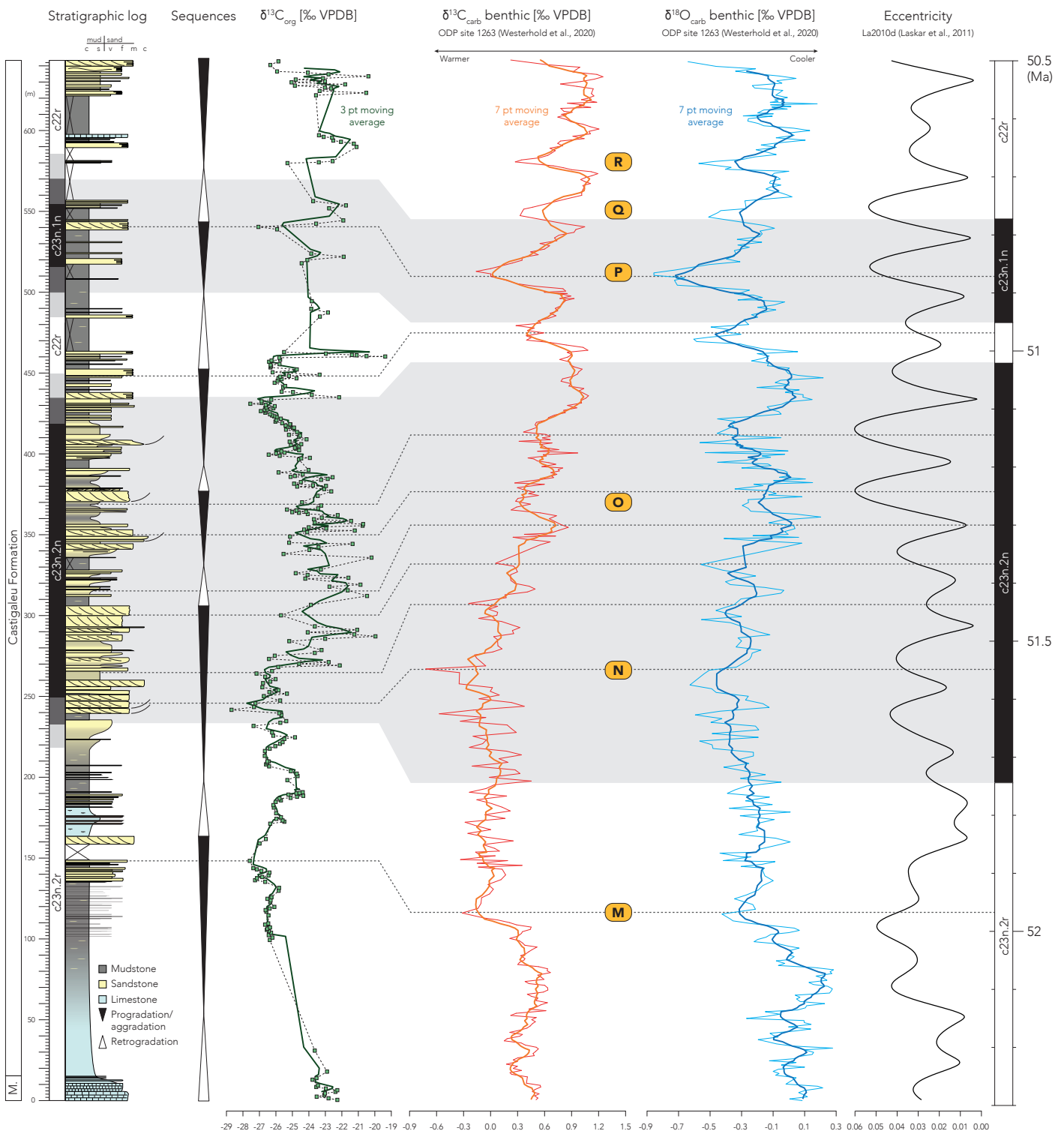


Figure 3. Stratigraphic log of the studied section along the Río Ésera with corresponding $\delta^{13}\text{C}_{\text{org}}$ values. The magnetic polarity zones are from [Bentham and Burbank \(1996\)](#). The main depositional sequences are shown. The dashed lines indicate a correlation between $\delta^{13}\text{C}_{\text{org}}$, $\delta^{13}\text{C}_{\text{carb}}$ and $\delta^{18}\text{O}_{\text{carb}}$ values ([Westerhold et al., 2020](#)) and eccentricity cycles ([Laskar et al., 2011](#)). The observed excursions towards more negative $\delta^{13}\text{C}_{\text{carb}}$ values are consistently linked with progradation/aggradation trends. Letters in yellow boxes denote hyperthermal events sensu [Westerhold et al. \(2020\)](#).

(Chanvry et al., 2018). Shallowing-upward trends are interpreted as progradation/aggradation sequences, while deepening-upward trends are considered retrogradation sequences, and are observed at different scales (Fig. 3) (Catuneanu et al., 2009; Chanvry et al., 2018).

The $\delta^{13}\text{C}_{\text{org}}$ values range from -28.7 to -19.4‰ , depicting several negative and positive CIEs at various scales (Fig. 3). TOC contents are relatively low, ranging from 0.02 to 1.49 wt%. Samples with TOC > 0.2 wt% have HI, OI, and T_{max} values spanning from 0 to 126.1 mg HC g⁻¹ TOC, 21.3 to 236.1 mg CO₂ g⁻¹ TOC, and 401.8 to 492°C, respectively (Supplemental Material). These values suggest that the organic matter present in the strata is terrestrially-dominated and mostly thermally immature to mature, limiting diagenetic overprint (Espitalie et al., 1985).

The statistical comparison of the $\delta^{13}\text{C}_{\text{org}}$ with TOC (Pearson correlation coefficient, $r = -0.25$), HI ($r = 0.11$), OI ($r = 0.18$), and T_{max} ($r = -0.09$) values, suggests no covariance among the data (Supplemental Material). The absence of correlation among the data indicates that the $\delta^{13}\text{C}_{\text{org}}$ profile is little influenced by potential lithological/source effects and likely largely reflects changes in the $\delta^{13}\text{C}_{\text{org}}$ composition of the atmosphere. The $\delta^{13}\text{C}_{\text{org}}$ trends persist even when considering only data from mudstone samples (Supplemental Material). Relying on the correspondences of magnetozones (c23n.2r, c23n.2n, c23n.1n, c22r; Fig. 3) between Bentham and Burbank (1996) and Westerhold et al. (2020), a tentative correlation between the measured $\delta^{13}\text{C}_{\text{org}}$ and coeval $\delta^{13}\text{C}_{\text{carb}}$ and $\delta^{18}\text{O}_{\text{carb}}$ reference records (Westerhold et al., 2020) are proposed (Fig. 3). This correlation allows us to estimate that the studied interval spans from ca. 52.2 to 50.6 Ma, covers a duration of ca. 1.6 Myr, and suggests a sedimentation rates of ca. 40 cm kyr⁻¹. The hyperthermal events M, N, O, P, Q, and R (Westerhold et al., 2020) occurred during this time interval (Fig. 3).

DISCUSSION AND CONCLUSION

The correspondence between the magnetozones allows to establish a correlation between the measured $\delta^{13}\text{C}_{\text{org}}$ and the $\delta^{13}\text{C}_{\text{carb}}$ reference record (Fig. 3), albeit with some discrepancies. Based on their stratigraphic positions and patterns, several negative CIEs are identified and associated with hyperthermal events (M, N, O, P; Fig. 3). These correlations are excellent, despite deltas being prone to erosion, reworking, and variable sediment discharge, which can lead to hiatuses or time-dilated intervals in the stratigraphy. These autogenic deltaic processes could explain the position of negative CIEs recorded in $\delta^{13}\text{C}_{\text{org}}$, either at the onset or the end of progradation and justify why $\delta^{13}\text{C}_{\text{org}}$ can exhibit discrepancies compared to $\delta^{13}\text{C}_{\text{carb}}$ without the need to infer an allogenic influence (Fig. 3). Furthermore, the differences in amplitude between the CIEs in $\delta^{13}\text{C}_{\text{org}}$ and $\delta^{13}\text{C}_{\text{carb}}$ may be attributed to local climate effects related to precipitation patterns that could distort the terrestrially-dominated $\delta^{13}\text{C}_{\text{org}}$ profile (Kohn, 2010). However, the exact origin of these discrepancies between $\delta^{13}\text{C}_{\text{org}}$ and $\delta^{13}\text{C}_{\text{carb}}$ falls beyond the scope of this

study, and shifts toward negative $\delta^{13}\text{C}_{\text{org}}$ remain associated with progradation/aggradation trends (Fig. 3).

During the Castigaleu Formation and coeval strata deposition, the SPFB evidences a continuous subsidence rate (Whitchurch et al., 2011; Chanvry et al., 2018), thus creating accommodation. Furthermore, ice-free conditions prevailed during the EECO (Westerhold et al., 2020) limiting the influence of sea level variations on the sedimentary system. Despite the anticipated retrogradation trend due to the increased accommodation (Jervey, 1988; Catuneanu et al., 2009; Neal and Abreu, 2009), the paleoenvironmental record of the Castigaleu Formation depicts contrasting trends (Fig. 3). Retrogradation and progradation trends are recorded (at both large and small scales), and consistently correlate with positive and negative CIEs, respectively (Fig. 3). The negative CIEs also align with maximum in eccentricity, which tend to intensify seasonal variations, enhancing hydrological cycles and the likelihood of extreme weather events, and vice versa (Walters et al., 2023). The retrogradation-progradation trends identified in this study are recorded in coeval strata along a depositional dip section (Chanvry et al., 2018). This regional correlation rules out the possibility that retrogradation-progradation trends result from autogenic deltaic processes.

The negative CIEs (Fig. 3), indicative of hyperthermal events during the EECO – similar to the PETM and the MECO – were linked to rapid increases in temperature that intensified precipitation and potentially triggered erosion and chemical weathering on land (Zachos et al., 2008). The hyperthermal events during the EECO could have enhanced hydrological cycles on land, increasing clastic sediment delivery to the ocean (t0, t2; Fig. 4). Negative CIEs occur in progradation/aggradation and suggest that $\delta A < \delta S$ (Fig. 4). Conversely, cooler intervals recorded by positive CIEs would have inhibited the hydrological cycle in the hinterland, decreasing clastic sediment flux into the basin and promoting fluvial aggradation. Coupled with continuous subsidence, the $\delta A > \delta S$ (t1; Fig. 4) led to the retrogradation of the system. This limited sediment flux into the basin explained the accumulation of carbonate-rich levels during retrogradation, reflecting reciprocal sedimentation sensu Zecchin and Catuneanu (2017). The record of these pulses of sediment supply is compatible with numerical simulation results indicating that sedimentary basins are more sensitive to short-term climate-induced δS rather than long-term tectonically-induced δS (Simpson and Castelltort, 2012). Furthermore, it is probable that the relatively short transfer zones in the SPFB (Fig. 1C) favored the direct source-to-sink transfer of $\delta^{13}\text{C}$ of sediment (Castelltort and Van Den Driessche, 2003; Vaucher et al., 2021).

In conclusion, our study of Early Eocene deltaic environments in the SPFB sheds light on the δS as a major control on sequence generation. This study, therefore, contributes to the broader understanding of the profound impact of climate change on shallow-marine systems, demonstrating the importance of considering sediment supply in the interpretation of depositional sequences.

Building of supply-driven delta sequences

Schematic stratigraphy

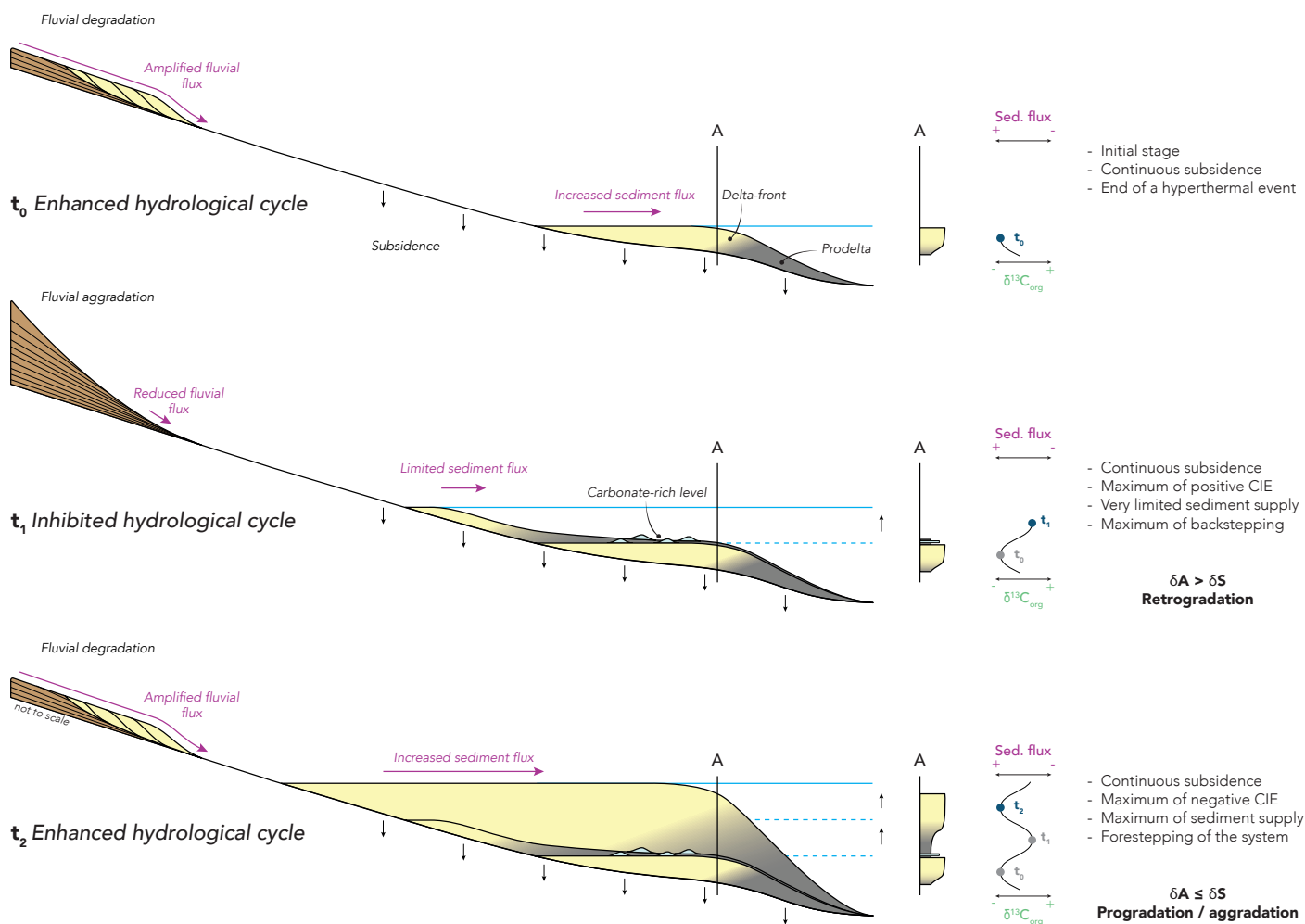


Figure 4. Conceptual model of supply-driven delta sequences during the Early Eocene in the South Pyrenean Foreland Basin. The studied section is marked as A. Stage t0 starts at the end of a hyperthermal event. Stage t1 is a phase of restricted sediment influx into the basin, manifested by the retrogradation of delta system, which favors the accumulation of carbonate layers in the basin. The siliciclastic sediment flux decreased as consequence of an inhibited hydrological cycle, resulting in the accumulation of sediment upstream. Stage t2 corresponds to a period characterized by a hyperthermal event that amplifies supply to the basin, resulting in a progradation/aggradation of the delta system.

ACKNOWLEDGMENTS

This research was funded through an SNSF grant to R.V. (P5R5PN_202846). Guillaume Suan and Tiffany Monnier are thanked for the feedback on the manuscript and the help in the laboratory, respectively.

REFERENCES CITED

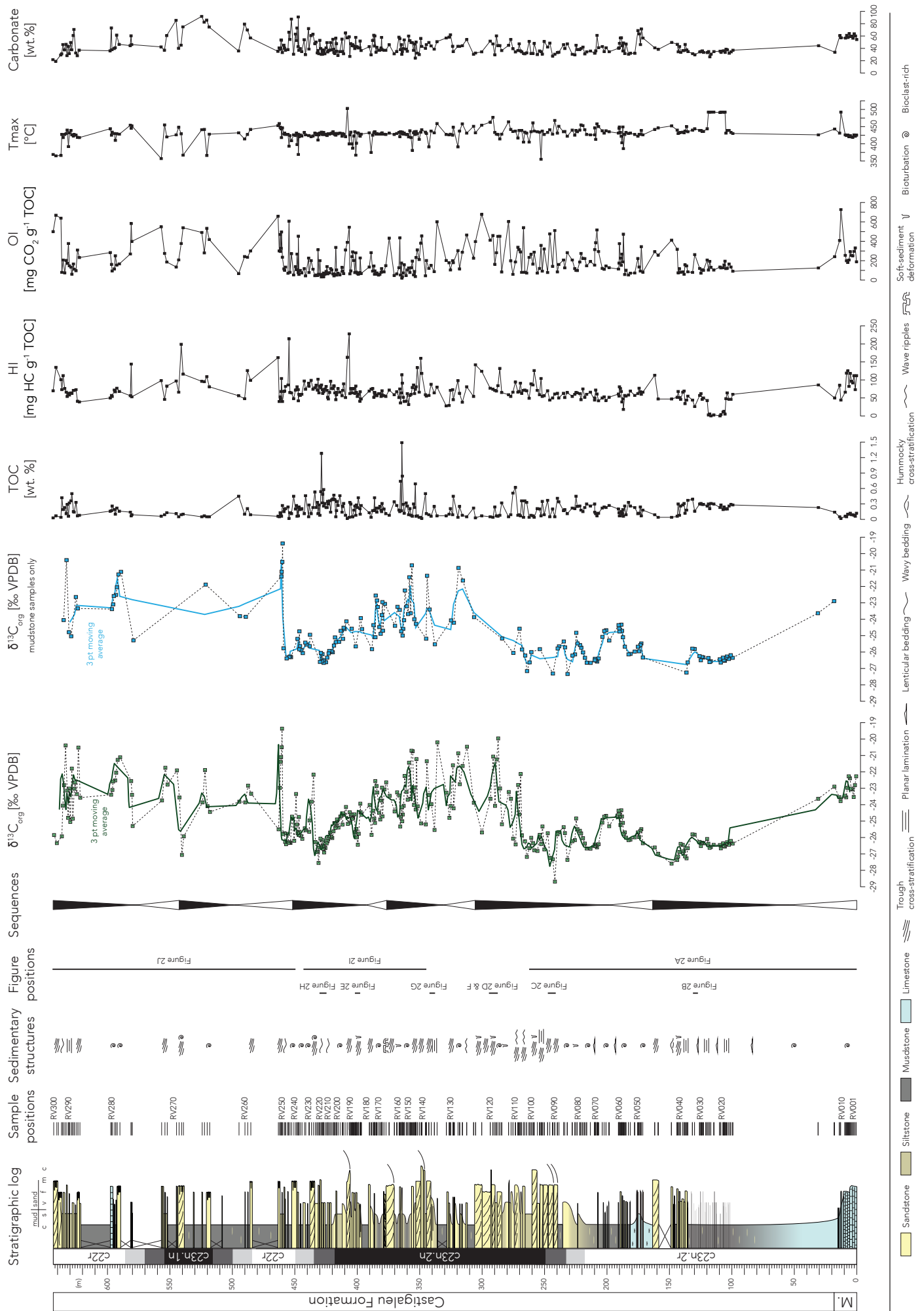
- Allen, P. A., Armitage, J. J., Carter, A., Duller, R. A., Michael, N. A., Sinclair, H. D., Whitchurch, A. L., and Whittaker, A. C., 2013, The Qs problem: Sediment volumetric balance of proximal foreland basin systems: *Sedimentology*, v. 60, p. 102-130, <https://doi.org/10.1111/sed.12015>.
- Bentham, P., and Burbank, D. W., 1996, Chronology of Eocene foreland basin evolution along the western oblique margin of the South-Central Pyrenees, in Dabrio, C. J., and Friend, P. F., eds., *Tertiary Basins of Spain: The Stratigraphic Record of Crustal Kinematics*: Cambridge, Cambridge University Press, p. 144-152, <https://doi.org/10.1017/CBO9780511524851.022>.
- Burgess, P. M., 2016, RESEARCH FOCUS: The future of the sequence stratigraphy paradigm: Dealing with a variable third dimension: *Geology*, v. 44, p. 335-336, <https://doi.org/10.1130/focus042016.1>.
- Burgess, P. M., and Prince, G. D., 2015, Non-unique stratal geometries: implications for sequence stratigraphic interpretations: *Basin Research*, v. 27, p. 351-365, <https://doi.org/10.1111/bre.12082>.
- Castelltort, S., Honegger, L., Adatte, T., Clark, J. D., Puigdefàbregas, C., Spangenberg, J. E., Dykstra, M. L., and Fildani, A., 2017, Detecting eustatic and tectonic signals with carbon isotopes in deep-marine strata, Eocene Ainsa Basin, Spanish Pyrenees: *Geology*, v. 45, p. 707-710, <https://doi.org/10.1130/g39068.1>.
- Castelltort, S., and Van Den Driessche, J., 2003, How plausible are high-frequency sediment supply-driven cycles in the stratigraphic record?: *Sedimentary Geology*, v. 157, p. 3-13, [https://doi.org/10.1016/S0037-0738\(03\)00066-6](https://doi.org/10.1016/S0037-0738(03)00066-6).
- Catuneanu, O., Abreu, V., Bhattacharya, J. P., Blum, M. D., Dalrymple, R. W., Eriksson, P. G., Fielding, C. R., Fisher, W. L., Galloway, W. E., Gibling, M. R., Giles, K. A., Holbrook, J. M., Jordan, R., Kendall, C. G. S. C., Macurda, B., Martinsen, O. J., Miall, A. D., Neal, J. E., Nummedal, D., Pomar, L., Posamentier, H. W., Pratt, B. R., Sarg, J. F., Shanley, K. W., Steel, R. J., Strasser, A., Tucker, M. E., and Winker, C., 2009, Towards the standardization of sequence stratigraphy: *Earth-Science Reviews*, v. 92, p. 1-33, <https://doi.org/10.1016/j.earscirev.2008.10.003>.
- Chanvry, E., Deschamps, R., Joseph, P., Puigdefàbregas, C., Poyatos-Moré, M., Serra-Kiel, J., Garcia, D., and Teinturier, S., 2018, The influence of intrabasinal tectonics in the stratigraphic evolution of piggyback basin fills: Towards a model from the Tremp-Graus-Ainsa Basin (South-Pyrenean Zone, Spain): *Sedimentary Geology*, v. 377, p. 34-62, <https://doi.org/10.1016/j.sedgeo.2018.09.007>.
- Chen, C., Guerit, L., Foreman, B. Z., Hassenruck-Gudipati, H. J., Adatte, T., Honegger, L., Perret, M., Sluijs, A., and Castelltort, S., 2018, Estimating regional flood discharge during Palaeocene-Eocene global warming: *Scientific Reports*, v. 8, p. 13391, <https://doi.org/10.1038/s41598-018-31076-3>.

- Espitalie, J., Deroo, G., and Marquis, F., 1985, La pyrolyse Rock-Eval et ses applications. Première partie: Rev. Inst. Fr. Pét., v. 40, p. 563-579, <https://doi.org/10.2516/ogst:1985035>.
- Ford, M., Masini, E., Vergés, J., Pik, R., Ternois, S., Léger, J., Dielforder, A., Frasca, G., Grool, A., Vinciguerra, C., Bernard, T., Angrand, P., Crémades, A., Manatschal, G., Chevrot, S., Jolivet, L., Mouthereau, F. d. r., Thinon, I., Calassou, S., Tavani, S., Teixell, A., Pedreira, D., and Calassou, S., 2022, Evolution of a low convergence collisional orogen: a review of Pyrenean orogenesis: BSGF - Earth Sciences Bulletin, v. 193, <https://doi.org/10.1051/bsgf/2022018>.
- Foreman, B. Z., Heller, P. L., and Clementz, M. T., 2012, Fluvial response to abrupt global warming at the Palaeocene/Eocene boundary: Nature, v. 491, p. 92-95, <https://doi.org/10.1038/nature11513>.
- Jervey, M. T., 1988, Quantitative Geological Modeling of Siliciclastic Rock Sequences and Their Seismic Expression, in Wilgus, C. K., Hastings, B. S., Posamentier, H., Wagoner, J. V., Ross, C. A., and Kendall, C. G. S. C., eds., Sea-Level Changes: An Integrated Approach, Volume 42, SEPM Society for Sedimentary Geology, p. 47-69, <https://doi.org/10.2110/pec.88.01.0047>.
- Khozyem, H., Adatte, T., Spangenberg, J. E., Tantawy, A. A., and Keller, G., 2013, Palaeoenvironmental and climatic changes during the Palaeocene–Eocene Thermal Maximum (PETM) at the Wadi Nukhul Section, Sinai, Egypt: Journal of the Geological Society, v. 170, p. 341-352, <https://doi.org/10.1144/jgs2012-046>.
- Kohn, M. J., 2010, Carbon isotope compositions of terrestrial C3 plants as indicators of (paleo)ecology and (paleo)climate: Proc Natl Acad Sci U S A, v. 107, p. 19691-19695, <https://doi.org/10.1073/pnas.1004933107>.
- Laskar, J., Fienga, A., Gastineau, M., and Manche, H., 2011, La2010: a new orbital solution for the long-term motion of the Earth: A&A, v. 532, p. A89, <https://doi.org/10.1051/0004-6361/201116836>.
- McCarren, H., Thomas, E., Hasegawa, T., Röhl, U., and Zachos, J. C., 2008, Depth dependency of the Paleocene-Eocene carbon isotope excursion: Paired benthic and terrestrial biomarker records (Ocean Drilling Program Leg 208, Walvis Ridge): Geochemistry, Geophysics, Geosystems, v. 9, <https://doi.org/10.1029/2008gc002116>.
- Muñoz, J.-A., Beamud, E., Fernández, O., Arbués, P., Dinarès-Turell, J., and Poblet, J., 2013, The Ainsa Fold and thrust oblique zone of the central Pyrenees: Kinematics of a curved contractional system from paleomagnetic and structural data: Tectonics, v. 32, p. 1142-1175, <https://doi.org/10.1002/tect.20070>.
- Muñoz, J. A., 1992, Evolution of a continental collision belt: ECORS-Pyrenees crustal balanced cross-section, in McClay, K. R., ed., Thrust Tectonics: Dordrecht, Springer Netherlands, p. 235-246, https://doi.org/10.1007/978-94-011-3066-0_21.
- Muto, T., and Steel, R. J., 1997, Principles of regression and transgression; the nature of the interplay between accommodation and sediment supply: Journal of Sedimentary Research, v. 67, p. 994-1000, <https://doi.org/10.1306/d42686a8-2b26-11d7-8648000102c1865d>.
- Neal, J., and Abreu, V., 2009, Sequence stratigraphy hierarchy and the accommodation succession method: Geology, v. 37, p. 779-782, <https://doi.org/10.1130/g25722a.1>.
- Payros, A., Tosquella, J., Bernaola, G., Dinarès-Turell, J., Orue-Etxebarria, X., and Pujalte, V., 2009, Filling the North European Early/Middle Eocene (Ypresian/Lutetian) boundary gap: Insights from the Pyrenean continental to deep-marine record: Palaeogeography, Palaeoclimatology, Palaeoecology, v. 280, p. 313-332, <https://doi.org/10.1016/j.palaeo.2009.06.018>.
- Peris Cabré, S., Valero, L., Spangenberg, J. E., Vinyoles, A., Verité, J., Adatte, T., Tremblin, M., Watkins, S., Sharma, N., Garcés, M., Puigdefàbregas, C., and Castellort, S., 2023, Fluvio-deltaic record of increased sediment transport during the Middle Eocene Climatic Optimum (MECO), Southern Pyrenees, Spain: Climate of the Past, v. 19, p. 533-554, <https://doi.org/10.5194/cp-19-533-2023>.
- Puigdefàbregas, C., and Souquet, P., 1986, Tecto-sedimentary cycles and depositional sequences of the Mesozoic and Tertiary from the Pyrenees: Tectonophysics, v. 129, p. 173-203, [https://doi.org/10.1016/0040-1951\(86\)90251-9](https://doi.org/10.1016/0040-1951(86)90251-9).
- Schlager, W., 1993, Accommodation and supply—a dual control on stratigraphic sequences: Sedimentary Geology, v. 86, p. 111-136, [https://doi.org/10.1016/0037-0738\(93\)90136-5](https://doi.org/10.1016/0037-0738(93)90136-5).
- Simpson, G., and Castellort, S., 2012, Model shows that rivers transmit high-frequency climate cycles to the sedimentary record: Geology, v. 40, p. 1131-1134, <https://doi.org/10.1130/g33451.1>.
- Spangenberg, J. E., 2016, Bulk C, H, O, and fatty acid C stable isotope analyses for purity assessment of vegetable oils from the southern and northern hemispheres: Rapid Communications in Mass Spectrometry, v. 30, p. 2447-2461, <https://doi.org/10.1002/rcm.7734>.
- Vaucher, R., Dashtgard, S. E., Horng, C.-S., Zeeden, C., Dillinger, A., Pan, Y.-Y., Setiaji, R. A., Chi, W.-R., and Löwemark, L., 2021, Insolation-paced sea level and sediment flux during the early Pleistocene in Southeast Asia: Scientific Reports, v. 11, p. 16707, <https://doi.org/10.1038/s41598-021-96372-x>.
- Vimpere, L., Spangenberg, J. E., Roige, M., Adatte, T., De Kaenel, E., Fildani, A., Clark, J., Sahoo, S., Bowman, A., Sternai, P., and Castellort, S., 2023, Carbon isotope and biostratigraphic evidence for an expanded Paleocene–Eocene Thermal Maximum sedimentary record in the deep Gulf of Mexico: Geology, v. 51, p. 334-339, <https://doi.org/10.1130/g50641.1>.
- Walters, A. P., Tierney, J. E., Zhu, J., Meyers, S. R., Graves, K., and Carroll, A. R., 2023, Climate system asymmetries drive eccentricity pacing of hydroclimate during the early Eocene greenhouse: Science Advances, v. 9, p. eadg8022, <https://doi.org/10.1126/sciadv.adg8022>.
- Westerhold, T., Marwan, N., Drury, A. J., Liebrand, D., Agnini, C., Anagnostou, E., Barnet, J. S. K., Bohaty, S. M., De Vleeschouwer, D., Florindo, F., Frederichs, T., Hodell, D. A., Holbourn, A. E., Kroon, D., Lauretano, V., Littler, K., Lourens, L. J., Lyle, M., Pälike, H., Röhl, U., Tian, J., Wilkens, R. H., Wilson, P. A., and Zachos, J. C., 2020, An astronomically dated record of Earth's climate and its predictability over the last 66 million years: Science, v. 369, p. 1383-1387, <https://doi.org/10.1126/science.aba6853>.
- Whitchurch, A. L., Carter, A., Sinclair, H. D., Duller, R. A., Whittaker, A. C., and Allen, P. A., 2011, Sediment routing system evolution within a diachronously uplifting orogen: Insights from detrital zircon thermochronological analyses from the South-Central Pyrenees: American Journal of Science, v. 311, p. 442-482, <https://doi.org/10.2475/05.2011.03>.
- Zachos, J. C., Dickens, G. R., and Zeebe, R. E., 2008, An early Cenozoic perspective on greenhouse warming and carbon-cycle dynamics: Nature, v. 451, p. 279-283, <https://doi.org/10.1038/nature06588>.
- Zecchin, M., and Catuneanu, O., 2017, High-resolution sequence stratigraphy of clastic shelves VI: Mixed siliciclastic-carbonate systems: Marine and Petroleum Geology, v. 88, p. 712-723, <https://doi.org/10.1016/j.marpetgeo.2017.09.012>.
- Zhang, J., Burgess, P. M., Granjeon, D., and Steel, R., 2019, Can sediment supply variations create sequences? Insights from stratigraphic forward modelling: Basin Research, v. 31, p. 274-289, <https://doi.org/10.1111/bre.12320>.

1 SUPPLEMENTAL MATERIAL

Two figures (Figures S1 and S2) and one table (Table S1) providing additional information about the stratigraphic log, including Rock-Eval pyrolysis and carbon isotope data.

Figure S1. Stratigraphic log of the 643.5 m thick studied section along the Río Ésera. The magnetostratigraphic zones are from [Benthams and Burbank \(1996\)](#). The sample positions, the main sedimentary structures, and the main depositional sequences are shown. The $\delta^{13}\text{C}_{\text{org}}$, the total organic carbon (TOC), the hydrogen index (HI), the oxygen index (OI), the T_{max} and the carbonate values are displayed. The $\delta^{13}\text{C}_{\text{org}}$ for the mudstone samples are plotted against the $\delta^{13}\text{C}_{\text{org}}$ for all samples and show similar trends, underlining no lithological effects on the $\delta^{13}\text{C}_{\text{org}}$ signals. ↓



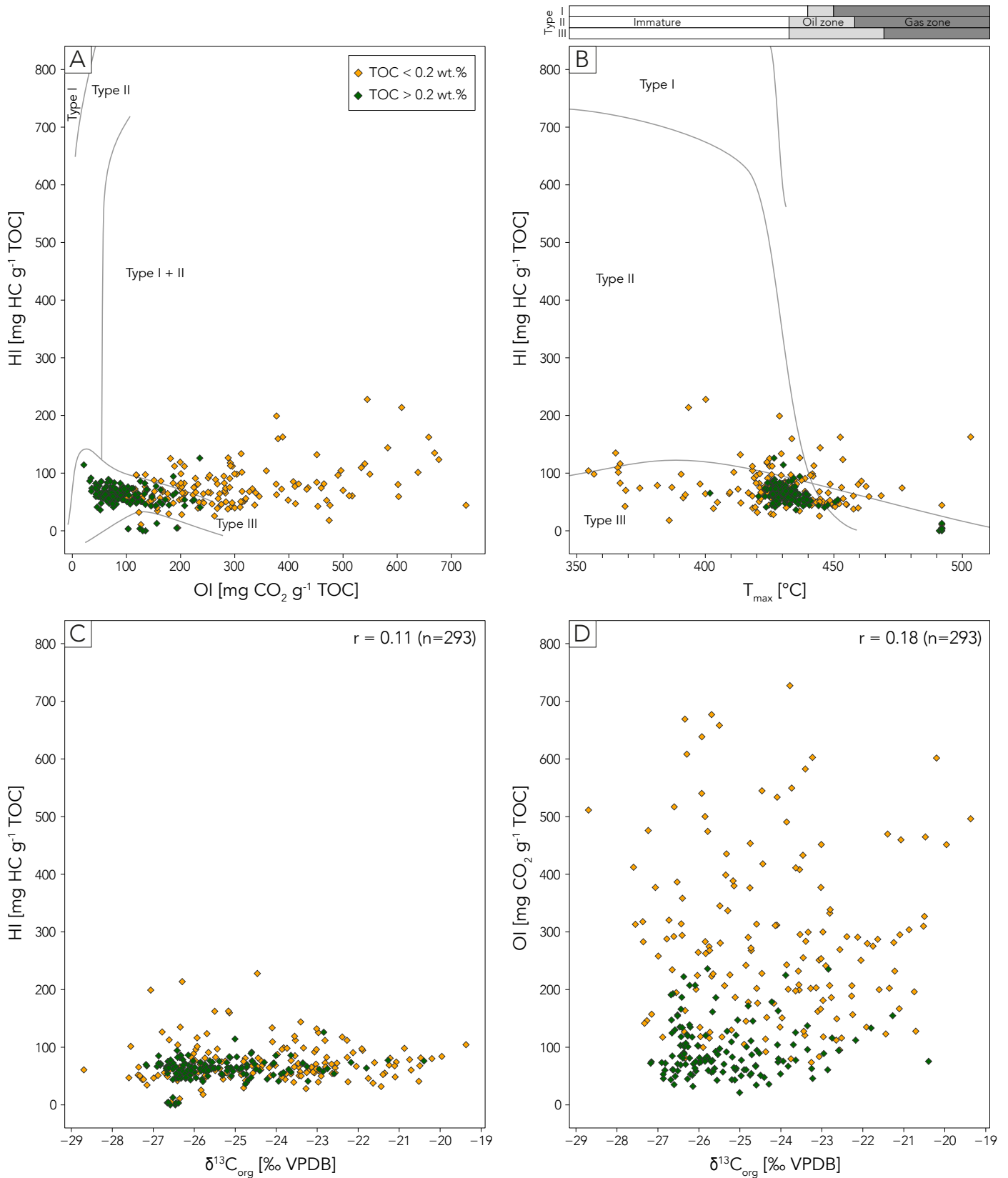


Figure S2. A) Hydrogen index (HI) versus oxygen index (OI) plot suggests that the organic matter is mostly of terrestrial origin (Type III). B) HI versus T_{max} plot show that organic matter preserved in the strata belong mostly to the immature zone and slightly to the mature zone, and point to low diagenetic effect. C) HI versus $\delta^{13}C_{org}$ plot and D) OI versus $\delta^{13}C_{org}$ plot show no covariance. Careful consideration should be taken for HI and OI data showing TOC < 0.2 wt.%.

Table S1. Río Ésera section stable isotope of total organic carbon ($\delta^{13}\text{C}_{\text{org}}$) and Rock-Eval data.

Sample	Position (m)	$\delta^{13}\text{C}_{\text{org}}$ [‰ VPDB]	TOC [w%]	HI [mg HC/g TOC]	OI [mg CO ₂ /g TOC]	Tmax [°C]	Carbonate [w%]
RV1	0.00	-22.27	0.12	112.04	188.78	425.00	54.26
RV2	1.00	-22.81	0.06	72.86	332.47	422.00	60.09
RV3	2.00	-23.53	0.08	112.10	295.57	426.00	63.68
RV4	3.00	-23.07	0.09	91.71	251.11	419.00	56.40
RV5	4.00	-23.02	0.09	96.20	253.65	420.00	59.54
RV6	5.00	-22.39	0.12	117.77	291.76	424.00	59.30
RV7	6.00	-22.27	0.10	82.36	206.72	421.00	63.89
RV8	7.00	-22.97	0.10	125.40	181.21	425.00	57.57
RV9	8.00	-23.55	0.05	119.07	199.23	424.00	61.15
RV10	9.00	-23.45	0.06	65.80	255.25	426.00	56.61
RV11	12.50	-23.78	0.02	44.26	727.12	492.00	57.20
RV12	13.50	-23.54	0.05	85.17	408.13	431.00	60.69
RV13	17.50	-22.90	0.14	50.00	241.21	443.00	33.81
RV14	30.50	-23.64	0.23	85.93	125.48	426.00	44.34
RV15	99.00	-26.37	0.28	60.35	90.72	430.00	37.04
RV16	100.50	-26.21	0.29	45.76	134.94	433.00	34.31
RV17	102.00	-26.44	0.26	46.45	166.04	439.00	32.04
RV18	103.50	-26.29	0.20	64.24	121.77	439.00	37.66
RV19	104.50	-26.43	0.21	47.97	118.21	431.00	38.71
RV20	105.25	-26.55	0.20	5.08	194.72	492.00	33.38
RV21	106.00	-26.52	0.24	12.82	156.03	492.00	35.94
RV22	106.75	-26.36	0.19	10.68	126.73	492.00	35.98
RV23	108.50	-26.66	0.28	3.60	124.75	492.00	33.39
RV24	109.25	-26.46	0.23	0.00	135.16	491.00	35.41
RV25	114.25	-26.45	0.30	3.33	103.20	492.00	34.85
RV26	116.50	-26.58	0.31	0.00	130.08	492.00	30.71
RV27	117.50	-26.63	0.21	4.69	192.82	492.00	26.44
RV28	118.50	-26.38	0.30	3.33	103.20	492.00	34.85
RV29	119.50	-26.09	0.26	43.47	207.43	444.07	33.03
RV30	122.50	-26.35	0.29	50.37	101.06	436.13	33.40
RV31	123.50	-26.32	0.29	46.41	106.88	436.20	36.01
RV32	124.50	-26.52	0.31	61.98	71.11	439.26	34.98
RV33	125.50	-26.27	0.30	57.37	119.68	439.33	34.22
RV34	129.50	-25.83	0.16	25.64	262.61	444.39	29.73
RV35	131.25	-25.81	0.39	44.49	78.72	440.46	31.40
RV36	135.00	-26.65	0.37	54.65	84.79	434.52	34.86
RV37	136.00	-27.27	0.18	44.12	146.12	449.59	37.49
RV38	137.25	-27.15	0.12	34.38	157.28	436.65	46.39
RV39	138.00	-26.83	0.31	68.98	60.17	431.72	36.50
RV40	139.00	-26.45	0.28	66.50	84.69	433.78	36.32
RV41	140.75	-26.39	0.26	46.21	81.31	432.85	33.46
RV42	141.75	-26.88	0.08	51.12	117.47	431.91	43.00
RV43	142.75	-27.16	0.30	67.65	74.71	429.98	34.41
RV44	143.50	-27.37	0.06	51.73	317.75	440.04	46.60
RV45	148.00	-27.59	0.04	47.03	412.17	452.11	49.67
RV46	158.75	-26.99	0.04	46.56	258.04	446.17	38.37
RV47	161.50	-26.61	0.09	112.82	292.12	442.24	40.85
RV48	171.00	-26.35	0.18	66.19	81.72	426.30	56.69
RV49	172.25	-25.49	0.07	59.58	345.20	439.37	71.42
RV50	173.00	-25.59	0.24	66.55	92.64	428.43	46.10
RV51	174.00	-25.97	0.12	76.63	134.51	426.50	63.51
RV52	175.00	-25.69	0.11	62.18	223.15	421.57	68.92
RV53	177.50	-25.99	0.23	56.81	73.26	426.63	31.95
RV54	181.00	-26.13	0.26	68.68	71.17	430.70	32.02
RV55	182.50	-26.16	0.33	58.32	51.59	429.76	30.53
RV56	184.50	-26.01	0.09	54.63	102.15	432.83	46.83
RV57	185.50	-25.69	0.26	56.73	56.64	426.89	31.65
RV58	186.60	-25.78	0.06	18.08	474.33	385.96	48.82
RV59	187.00	-25.11	0.19	47.95	186.55	449.04	35.92
RV60	187.75	-24.72	0.10	38.64	267.66	403.17	44.34
RV61	188.30	-24.34	0.15	68.27	151.71	422.30	57.24
RV62	189.00	-25.24	0.07	75.96	225.61	433.43	56.88
RV63	189.75	-24.76	0.07	80.93	376.48	448.57	48.10
RV64	190.00	-24.57	0.13	55.19	176.46	444.70	40.96
RV65	190.50	-24.37	0.20	61.06	114.17	430.83	40.29
RV66	198.00	-25.31	0.27	51.58	127.76	434.96	34.54
RV67	200.50	-24.68	0.23	43.00	145.41	438.09	40.98
RV68	202.00	-24.73	0.24	52.85	111.02	431.22	34.73
RV69	203.50	-25.09	0.22	50.30	120.87	438.35	43.00
RV70	206.50	-26.41	0.12	41.99	294.06	450.48	41.09
RV72	207.75	-26.60	0.07	60.55	516.91	457.61	61.08
RV73	208.75	-26.53	0.11	72.26	386.50	412.74	36.10

RV74	209.50	-26.43	0.14	50.13	314.05	445.87	32.47
RV75	209.60	-26.52	0.30	43.96	154.31	426.00	32.08
RV76	213.00	-26.68	0.26	65.86	190.94	426.00	35.69
RV77	216.00	-26.67	0.30	60.49	147.22	427.00	34.20
RV78	217.50	-26.37	0.23	52.20	222.32	441.00	30.94
RV79	219.00	-26.04	0.15	75.16	224.50	453.00	42.09
RV80	220.50	-25.75	0.18	45.41	274.56	455.00	39.84
RV81	221.50	-25.59	0.26	61.96	186.04	439.98	38.24
RV82	223.50	-25.49	0.25	63.70	97.58	434.96	38.22
RV83	224.50	-24.84	0.45	65.23	100.50	438.93	45.07
RV84	225.50	-26.16	0.21	60.03	117.68	424.91	29.57
RV85	227.50	-26.23	0.22	53.75	207.33	439.89	30.41
RV86	231.50	-27.36	0.11	65.46	282.87	421.87	47.35
RV87	233.50	-25.73	0.19	51.23	125.99	435.85	39.68
RV88	234.50	-25.37	0.17	63.24	206.78	434.83	45.99
RV89	238.30	-25.67	0.34	50.04	161.40	450.52	33.78
RV90	239.40	-25.80	0.41	63.29	84.04	431.43	33.02
RV91	241.50	-28.69	0.05	60.82	511.33	468.41	30.53
RV92	243.25	-27.33	0.20	50.45	141.51	428.39	27.64
RV93	245.50	-27.24	0.05	44.21	475.86	441.37	48.59
RV94	247.25	-25.74	0.37	70.02	78.21	433.35	42.13
RV95	250.00	-26.73	0.09	55.95	320.44	426.65	51.07
RV96	251.50	-25.33	0.35	53.93	91.96	436.61	30.81
RV97	252.50	-26.40	0.07	104.03	358.38	354.57	34.60
RV98	253.70	-25.84	0.20	58.70	120.46	433.80	35.91
RV99	255.50	-26.82	0.21	71.46	72.25	434.78	29.90
RV100	258.00	-26.78	0.04	126.46	287.87	436.76	47.87
RV101	259.00	-26.34	0.07	86.25	163.72	460.74	31.74
RV102	260.50	-26.02	0.08	88.64	264.58	434.72	31.74
RV103	262.00	-26.65	0.04	49.33	234.40	404.70	51.28
RV104	264.00	-27.18	0.33	69.97	72.24	430.89	32.71
RV105	265.50	-26.23	0.36	72.17	81.20	433.87	31.11
RV107	268.00	-25.86	0.36	62.68	79.89	438.83	34.26
RV108	269.00	-22.13	0.07	90.61	290.83	438.80	35.98
RV109	270.00	-24.59	0.09	68.31	313.56	438.78	47.43
RV110	271.00	-22.80	0.08	65.80	338.65	416.76	36.47
RV111	273.00	-26.42	0.62	94.26	186.66	436.74	34.16
RV112	275.00	-26.07	0.51	65.63	58.66	435.72	39.38
RV113	276.75	-23.64	0.09	53.62	197.73	441.70	54.54
RV114	278.50	-23.23	0.05	59.37	602.63	463.67	44.90
RV115	284.00	-25.19	0.32	65.06	82.99	427.65	36.40
RV116	285.50	-23.01	0.08	132.00	451.60	413.63	44.53
RV117	287.00	-19.96	0.06	84.09	451.42	426.61	44.49
RV118	288.20	-21.24	0.07	69.06	281.53	427.59	60.28
RV119	289.50	-24.07	0.24	71.18	163.11	432.57	29.66
RV120	291.00	-21.07	0.04	74.28	459.73	476.54	47.20
RV121	293.20	-23.64	0.05	76.94	411.15	462.52	51.77
RV122	300.00	-25.69	0.07	123.56	676.91	453.50	34.36
RV124	306.50	-23.88	0.22	53.62	224.93	451.46	30.34
RV125	312.00	-20.47	0.05	81.45	464.74	430.67	54.27
RV126	315.50	-21.64	0.08	37.73	287.24	457.65	44.31
RV127	317.75	-22.75	0.25	62.89	116.04	436.63	43.14
RV128	319.00	-20.87	0.04	98.11	303.86	390.61	43.38
RV130	322.75	-24.22	0.45	44.60	178.64	447.59	34.77
RV131	323.25	-21.60	0.09	73.33	199.93	424.57	43.51
RV132	325.00	-24.08	0.21	71.15	104.17	427.54	61.99
RV133	326.10	-24.79	0.10	29.45	178.18	425.52	58.30
RV134	328.40	-23.27	0.07	28.19	202.11	426.50	56.81
RV135	335.75	-20.20	0.07	80.27	601.57	459.48	50.98
RV136	338.00	-25.54	0.25	63.57	87.49	432.46	38.70
RV137	340.50	-23.97	0.06	87.54	150.96	437.43	44.00
RV138	342.25	-23.41	0.09	57.24	120.72	391.41	49.61
RV139	344.25	-21.35	0.11	55.06	202.45	430.39	45.94
RV140	345.00	-25.20	0.50	59.32	43.65	434.37	40.23
RV142	348.75	-25.14	0.04	159.69	379.93	433.65	56.18
RV144	351.50	-24.10	0.07	133.70	311.86	429.57	32.25
RV145	352.50	-21.22	0.06	80.95	232.03	435.52	50.16
RV146	353.10	-24.29	0.69	73.75	35.97	427.48	24.38
RV147	353.75	-22.95	0.23	61.96	89.03	435.43	46.96
RV148	354.50	-24.01	0.30	85.59	53.68	432.39	36.91
RV149	355.50	-20.74	0.06	78.56	196.21	381.35	49.17
RV150	356.50	-20.71	0.08	60.38	127.77	418.30	49.59
RV151	357.45	-23.64	0.21	56.88	77.60	438.26	52.66
RV152	358.45	-21.44	0.09	31.90	123.03	420.22	60.02
RV153	359.50	-23.69	0.26	61.76	104.35	427.17	35.27

RV154	360.50	-23.22	0.32	41.06	45.81	427.13	38.77
RV155	362.00	-22.25	0.12	40.03	156.59	431.48	53.76
RV156	362.75	-24.07	0.29	51.91	74.28	428.43	39.41
RV157	363.50	-24.60	0.84	91.42	34.42	434.39	34.94
RV158	363.90	-25.01	1.49	114.32	21.30	430.35	30.27
RV159	364.20	-24.17	0.17	64.49	176.12	434.30	45.84
RV160	365.00	-24.75	0.74	36.21	51.72	435.26	38.00
RV161	365.50	-25.33	0.15	74.72	435.37	421.22	55.74
RV162	366.20	-23.44	0.18	50.67	127.60	433.17	58.19
RV163	368.00	-23.25	0.27	66.52	62.94	430.13	35.06
RV164	370.00	-24.41	0.34	59.21	47.71	427.09	31.11
RV165	374.00	-23.46	0.08	71.97	432.98	431.04	45.86
RV166	376.75	-22.64	0.11	54.44	149.31	427.09	36.86
RV167	378.20	-23.07	0.20	55.84	83.65	428.04	36.87
RV168	379.75	-24.71	0.31	69.67	87.02	432.04	38.26
RV169	380.10	-22.96	0.15	59.21	118.07	428.09	57.79
RV170	380.50	-23.75	0.18	54.11	79.88	429.13	40.41
RV171	381.50	-24.90	0.25	61.73	60.95	428.17	37.04
RV172	382.50	-24.49	0.22	62.09	51.32	428.22	36.97
RV173	383.90	-23.26	0.14	56.10	73.68	430.26	41.61
RV174	384.50	-22.86	0.22	57.98	60.84	428.30	33.93
RV175	385.50	-22.56	0.18	64.01	95.06	435.35	60.10
RV176	385.75	-25.11	0.42	64.94	60.70	435.39	43.72
RV177	386.30	-24.85	0.17	52.03	145.10	432.43	61.35
RV178	387.25	-24.37	0.17	76.42	92.10	425.48	52.94
RV179	388.50	-25.84	0.04	74.02	283.13	374.52	29.62
RV180	390.00	-24.02	0.13	68.54	134.91	431.57	42.72
RV181	396.50	-24.61	0.27	47.35	68.23	427.61	36.46
RV182	397.25	-24.46	0.10	66.76	228.02	421.65	51.94
RV183	397.50	-23.94	0.21	41.06	75.78	423.70	40.91
RV184	398.75	-25.77	0.42	59.95	59.78	430.74	40.60
RV185	399.50	-26.44	0.23	54.37	69.32	431.78	42.26
RV186	400.25	-25.99	0.28	65.25	81.72	401.83	43.03
RV187	400.75	-25.48	0.08	82.68	280.72	366.87	57.85
RV188	401.50	-25.67	0.26	63.40	76.98	434.91	39.64
RV189	402.25	-24.59	0.18	76.24	202.08	422.96	43.69
RV190	403.25	-24.80	0.05	75.25	290.54	387.00	46.08
RV191	403.75	-24.85	0.05	64.20	242.10	400.04	44.37
RV192	404.75	-24.59	0.30	75.70	94.65	434.09	47.80
RV193	405.50	-25.09	0.33	61.95	63.56	426.13	26.88
RV194	406.00	-24.46	0.04	227.85	544.76	400.17	58.56
RV195	407.50	-25.17	0.02	162.71	388.55	503.22	57.05
RV196	409.00	-24.14	0.08	50.62	311.11	420.96	64.88
RV197	410.50	-24.61	0.31	89.21	66.79	426.93	31.20
RV198	411.25	-24.53	0.25	70.77	89.68	429.91	34.97
RV199	411.75	-25.21	0.14	55.57	129.79	421.57	55.08
RV200	413.50	-24.72	0.46	65.68	54.52	430.61	34.84
RV201	415.00	-25.39	0.27	75.67	70.64	428.65	28.60
RV202	416.00	-24.97	0.35	65.36	50.52	429.70	35.17
RV203	416.20	-24.90	0.17	59.10	105.04	429.74	47.79
RV204	416.75	-25.29	0.05	44.62	336.86	424.78	56.40
RV205	417.50	-25.41	0.38	64.23	57.04	426.83	31.89
RV206	418.20	-25.12	0.39	82.06	43.25	429.87	33.29
RV207	418.30	-25.14	0.47	83.59	64.67	428.91	38.40
RV208	419.00	-25.62	0.40	76.43	63.29	434.96	54.77
RV209	420.00	-26.03	0.38	76.23	102.80	430.98	37.44
RV210	420.90	-25.96	0.14	96.22	118.56	429.52	49.47
RV211	421.75	-25.70	0.36	64.52	74.88	427.54	37.15
RV212	422.75	-25.95	0.30	46.81	74.37	428.57	35.91
RV213	423.25	-26.10	0.35	51.63	63.78	427.59	34.12
RV214	423.75	-26.23	0.23	71.39	138.90	423.61	49.38
RV215	424.50	-26.36	0.23	82.34	88.63	425.63	40.76
RV216	425.50	-26.64	0.31	75.39	61.20	427.65	31.18
RV217	426.50	-26.91	0.26	66.65	73.36	427.35	37.35
RV218	426.50	-26.61	0.58	68.60	35.14	433.39	35.91
RV219	427.25	-26.68	0.49	63.35	43.68	430.43	30.69
RV220	427.50	-26.52	0.32	72.76	59.14	427.48	36.12
RV221	428.25	-26.15	1.28	86.30	32.12	433.52	30.17
RV222	428.75	-26.58	0.54	77.86	49.67	430.02	39.87
RV223	429.50	-26.07	0.08	82.70	200.47	431.04	53.06
RV224	430.25	-26.62	0.28	64.34	60.64	426.07	31.28
RV225	431.00	-27.55	0.11	101.54	313.16	411.09	36.56
RV226	431.50	-26.87	0.33	72.25	45.68	429.11	32.63
RV227	432.50	-26.87	0.23	85.08	53.15	426.13	50.09
RV228	433.50	-26.28	0.53	78.41	44.98	431.15	47.76

RV229	435.00	-22.17	0.23	73.71	112.18	423.17	62.84
RV230	436.50	-23.82	0.11	98.95	200.62	421.20	60.62
RV231	438.20	-24.96	0.28	83.34	77.56	424.22	38.84
RV232	438.50	-25.65	0.05	91.03	227.29	424.24	72.16
RV233	441.00	-25.56	0.46	74.02	42.71	426.26	29.79
RV234	442.00	-25.44	0.11	96.99	117.90	433.28	54.08
RV235	444.00	-26.08	0.21	59.66	75.05	423.26	34.80
RV236	445.25	-25.90	0.19	56.58	99.78	426.30	39.80
RV237	446.25	-25.65	0.24	59.78	57.93	420.70	37.17
RV238	446.75	-24.75	0.07	42.37	453.48	368.78	90.92
RV239	446.85	-25.85	0.23	73.26	75.70	427.87	42.67
RV240	447.75	-25.74	0.06	81.21	267.89	397.96	73.08
RV241	448.25	-25.21	0.27	73.34	109.36	431.04	52.69
RV242	449.00	-23.35	0.20	71.62	137.16	424.13	63.12
RV243	450.50	-26.20	0.45	47.64	53.18	426.22	30.59
RV244	452.25	-24.73	0.11	64.31	272.02	409.30	87.43
RV245	453.50	-26.33	0.13	65.39	81.40	424.39	54.38
RV246	454.20	-26.29	0.02	213.82	608.28	393.48	66.04
RV247	455.00	-26.32	0.24	85.79	70.39	426.57	38.05
RV249	457.00	-26.41	0.21	82.36	133.87	427.30	36.82
RV250	457.75	-26.27	0.20	68.93	100.92	431.33	40.40
RV251	458.25	-25.74	0.15	68.38	115.77	428.35	45.21
RV252	459.50	-25.79	0.27	40.49	236.13	446.37	33.15
RV253	460.25	-19.37	0.06	104.44	496.21	418.39	53.18
RV254	460.50	-20.50	0.07	67.97	326.93	444.41	53.74
RV255	461.00	-21.10	0.12	48.50	295.11	447.43	38.30
RV256	461.25	-21.39	0.13	52.76	469.73	448.46	40.48
RV257	462.00	-22.97	0.05	39.64	299.92	459.48	40.80
RV258	463.00	-25.50	0.06	162.33	658.22	452.50	35.09
RV259	485.00	-23.33	0.09	98.78	299.61	441.65	56.87
RV260	487.50	-22.84	0.21	126.04	235.41	426.74	69.90
RV261	489.75	-23.86	0.10	48.29	242.93	413.83	79.41
RV262	494.50	-23.82	0.45	56.04	67.06	431.91	35.86
RV263	518.00	-24.44	0.05	81.24	418.02	427.97	74.53
RV264	520.00	-24.09	0.05	109.43	533.67	365.95	85.87
RV265	522.00	-21.89	0.07	94.71	279.88	441.92	82.57
RV266	524.00	-23.86	0.05	96.39	490.61	440.90	91.87
RV267	539.00	-25.93	0.10	116.28	540.22	366.87	74.85
RV268	540.50	-27.06	0.09	199.06	377.15	428.85	45.16
RV269	542.50	-23.56	0.05	65.82	208.34	447.82	40.17
RV270	544.50	-21.91	0.11	97.40	134.87	425.79	85.50
RV271	552.00	-22.77	0.13	82.54	186.19	419.77	60.68
RV272	553.80	-21.75	0.09	46.03	275.28	454.74	37.15
RV273	556.50	-23.74	0.06	98.21	549.49	356.72	42.41
RV274	580.00	-25.34	0.09	53.16	398.71	451.69	46.11
RV275	580.50	-23.40	0.07	143.90	582.55	444.67	60.40
RV276	581.20	-22.56	0.14	55.76	269.40	453.64	44.53
RV277	590.00	-21.11	0.16	67.66	166.82	427.62	46.47
RV278	592.00	-21.27	0.22	77.40	154.72	428.59	61.57
RV279	593.20	-22.05	0.10	66.80	250.79	409.56	41.04
RV280	594.00	-22.52	0.19	72.40	116.05	429.54	39.63
RV281	595.75	-22.59	0.26	54.09	94.47	433.51	37.88
RV282	596.25	-23.10	0.17	57.00	162.07	425.49	73.20
RV283	597.25	-23.39	0.16	50.20	283.70	444.46	36.11
RV284	622.00	-23.57	0.08	39.25	232.01	418.44	37.18
RV285	623.50	-20.52	0.07	40.93	309.92	419.41	28.00
RV286	624.70	-23.35	0.33	72.69	95.96	425.38	32.55
RV287	626.20	-22.65	0.14	70.72	112.30	427.36	70.70
RV288	626.75	-23.03	0.15	70.71	166.27	423.33	60.79
RV289	628.00	-24.85	0.50	63.11	60.97	426.31	37.70
RV290	628.75	-21.80	0.36	63.91	133.32	439.28	49.54
RV291	630.00	-25.05	0.32	58.15	147.18	432.26	31.45
RV292	630.75	-23.02	0.06	62.59	377.17	392.23	43.53
RV293	631.75	-24.80	0.29	53.93	171.66	439.50	28.14
RV294	632.50	-23.14	0.11	65.62	203.17	430.44	46.61
RV295	633.75	-20.39	0.23	76.17	75.47	427.38	37.44
RV296	635.00	-22.81	0.19	111.84	207.02	418.31	46.22
RV297	636.00	-24.06	0.42	72.71	79.95	427.25	31.06
RV298	636.75	-25.93	0.04	101.31	638.48	366.19	29.22
RV300	640.75	-26.34	0.07	134.94	669.05	365.13	19.06
RV301	643.00	-25.85	0.03	70.05	500.14	369.06	21.67